



**HAL**  
open science

# An efficient computational model for fluid-structure interaction in application to large overall motion of wind turbine with flexible blades

Abir Boujleben, Adnan Ibrahimbegovic, Emmanuel Lefrançois

## ► To cite this version:

Abir Boujleben, Adnan Ibrahimbegovic, Emmanuel Lefrançois. An efficient computational model for fluid-structure interaction in application to large overall motion of wind turbine with flexible blades. Applied Mathematical Modelling, 2020, 77, pp.392-407. 10.1016/j.apm.2019.07.033 . hal-02433808

**HAL Id: hal-02433808**

**<https://hal.utc.fr/hal-02433808>**

Submitted on 20 Dec 2021

**HAL** is a multi-disciplinary open access archive for the deposit and dissemination of scientific research documents, whether they are published or not. The documents may come from teaching and research institutions in France or abroad, or from public or private research centers.

L'archive ouverte pluridisciplinaire **HAL**, est destinée au dépôt et à la diffusion de documents scientifiques de niveau recherche, publiés ou non, émanant des établissements d'enseignement et de recherche français ou étrangers, des laboratoires publics ou privés.



Distributed under a Creative Commons Attribution - NonCommercial 4.0 International License

# An efficient computational model for fluid-structure interaction in application to large overall motion of wind turbine with flexible blades

Abir Boujleben\*, Adnan Ibrahimbegovic, Emmanuel Lefrançois

*Université de Technologie de Compiègne - Sorbonne Universités, , Laboratoire Roberval de Mécanique, Chair for Computational Mechanics, 60205 Compiègne, France*

---

## Abstract

This paper proposes a very efficient computational model for fluid-structure interaction problems corresponding to steady-state flow representing a large overall motion of wind turbines with flexible blades. The model of turbine blades is based upon the 3D solids finite elements with drilling rotations. The proposed 3D solids model is fully able to describe the flexibility blades large overall motion and easily capture both bending and torsional motion thanks to using an enhanced strain field. The model efficiency is further reinforced by using the 3D panel method that fits naturally with proposed 3D solid finite elements for blades. The proposed panel method is the corresponding modification of the potential fluid flow by introducing a vorticity layer at the fluid-structure interface and Bernoulli's conservation momentum equation in order to provide quantification for the blade thrust. The fluid-structure interaction is enforced through an efficient iterative procedure providing on one hand a very fast computation of aerodynamic loads, which is sufficiently accurate for computing the overall thrust on the blade, and on the other hand a sufficiently accurate representation of the stress states suitable for fatigue studies. The proposed computational model performance is illustrated with several numerical simulations, including the practical case of a full-scale NREL 5MW wind turbine.

---

\*Corresponding author

*Email address:* [abir.boujeleben@utc.fr](mailto:abir.boujeleben@utc.fr) (Abir Boujleben)

*Keywords:* fluid-structure interaction, 3D vortex panel method, large overall motion, follower pressure, wind turbine blades.

---

## 1. Introduction

The current push for renewable energy resources is the main motivation for constructing large wind turbines. The development of such wind turbines with very large blades requires to take into account the blade flexibility in order to provide a good understanding of the coupling effects between the blades large motion and the corresponding aerodynamics. Hence, FSI (fluid-structure interaction) simulations are essential for accurate modeling of these wind turbines. FSI simulations can be classified according to the direction of coupling. The one-way coupling is to transfer only the loads calculated with fluid solver into structural domain with no influence of the structure motion. This coupling approach is studied in our previous work [1]. It can not capture an accurate interaction in the sense that the motion and deformation of the wind turbine blades depend on the wind speed and airflow, as much as the aerodynamic loads depend on the motion and deformation of the blades. Thus, the two-ways coupling is developed in this paper taking account of the interaction between the blade motion and deformations and the aerodynamic pressure, with the main goal of achieving both efficiency and sufficient accuracy.

In the two-ways coupling case, two approaches can be distinguished: monolithic and partitioned. In the monolithic approach, the fluid equations and the structural equations are incorporated with a common system, formulated and solved as one single entity (e.g. see [2, 3]). On the other hand, the partitioned approach is to solve the fluid equations and the structural equations separately and to achieve the interaction by exchanging the common data through the fluid-structure interface (e.g. [4, 5]). This approach is capable of using different, possibly more efficient, solution techniques for both fluid and structural computations. Therefore, due to the size and the complexity of the problem, we adopt partitioned coupling in this work. [The main challenge remains to extend the](#)

partitioned coupling of FSI problems in the presence of large overall motion of flexible blades, especially that the proposed structural model enforces the path dependency with large rotations and thus imposes the Lagrangian approach. The latter will be combined with the Eulerian approach for the proposed fluid model.

There are essentially three approaches to model the aerodynamic behavior of wind turbines. The blade element momentum (BEM) theory, initially proposed by Glauert [6], is a fast and easily implemented method, but it is restricted to 2D flow and assumes that each blade section is independent of every other blade section. The computational fluid dynamics (CFD), governed by the Navier-Stokes equations, is considered to be the most accurate, but also by far the most costly [2, 7]. Moreover, a special attention should be given to problems related to the data transfer in the fluid-structure interface [8], the volume mesh updating of the fluid domain and the choice of numerical integration parameters in Navier-Stokes resolution. The vortex panel method (VPM) [9] combines the advantages of the BEM and CFD. It is faster than CFD, as it doesn't need to solve the full Navier-Stokes equations and is able to handle more complicated cases than BEM for 3D problems. It provides the aerodynamic pressure distribution over entire blade surface which is suitable for structural model. The standard VPM is restricted for non-lifting potential flow. In this paper, It is modified to account for flexible lifting body in large overall motion by introducing vorticity at fluid-structure interface and by considering the relative flow velocity.

The novelty also concerns the structure model computations with respect to the standard finite element method (FEM). Namely, the wind turbine blades are the most frequently described by beam [10] or shell models (e.g. [11]), since the models of this kind allow to save the computational time. Here, we choose the 3D solid model which allows more rigorous stress distribution that is of special interest for fatigue failure, as the most common problem for wind turbines. An enhanced 8-node solid element for the blade dynamics model is used with a special choice of the deformation measure for more accurate approximation of bending and torsional deflections. The formulation developments and the finite

element implementation of the proposed solid element are presented in details in our previous work [12]. An additional advantage of such choice is that the structure discretization is identical to panel method discretization, eliminating all inaccuracy related to the data transfer at the fluid-structure interface. The coupling between panel method and enhanced 3D solid element offers a good compromise between the process rapidity and the approximation quality. It is very suitable to the parametric studies in preliminary design phase.

The final concern is the robustness of the partitioned fluid-structure interaction solution procedures. Several algorithms of partitioned computational procedure are currently used, such as conventional serial staggered procedure (CSS) [13]. A basic implementation of CSS reduces the time of coupling computation. However, it does not ensure the displacement continuity and the quality of the coupling. Several improved procedures have been proposed by introducing a structure displacement predictor in updating phase of the fluid mesh and a aerodynamic load corrector in advancing the structural solution to the next step. The choice of the prediction remains unsettled issue. In this paper, an iterative coupling algorithm is carried out until convergence to exchange in each time step the aerodynamic loads (panel method code) and the structure displacements and velocities (FEM approximation) at the fluid-structure interface. [Some considerations are taken into account to ensure reliable interaction between structural and fluid codes in large displacements and deformations theory.](#)

The paper outline is as follows. Section 2 describes the FSI problem. We first present the procedure to compute the unioitile fluid flow loads based on the 3D vortex panel method. Then we detail the blade structural model based on a variational formulation of the 3D solid element with independent rotational degrees of freedom. Finally, we present the implementation of the strong coupling between fluid and solid models. Several illustrative numerical simulations and their results discussions are given in Section 3. The model is also used to test new configurations, in terms of blade geometry and flow direction. Some closing remarks are given in Section 4.

## 2. Problem statement

### 2.1. Fluid flow computations by 3D vortex panel method

In this section we discuss the 3D panel method which is used to predict the aerodynamic pressure applied on the blade surface [14, 15, 9]. We start by first considering the steady-state potential flow, imposing the requirements of incompressibility and irrotational motion by enforcing the following fluid velocity field constraints:

$$\nabla \cdot \mathbf{v}^f = 0 \text{ (incompressible); } \nabla \times \mathbf{v}^f = \mathbf{0} \text{ (irrotational)} \quad (1)$$

where superscript ' $f$ ' indicates fluid.

By using the Helmholtz decomposition [16], the velocity field can be written as the sum of the gradient of a scalar potential  $\phi$  and the curl of a vector potential  $\psi$ :

$$\mathbf{v}^f = \nabla\phi + \nabla \times \psi \quad (2)$$

By substituting such velocity definition in (2) into the incompressibility condition (1)<sub>1</sub> leads to the Laplace equation of the scalar potential:

$$\nabla \cdot \mathbf{v}^f = \nabla \cdot (\nabla\phi + \nabla \times \psi) = \nabla^2\phi = 0 \quad (3)$$

The vector potential  $\psi$  is introduced in order to generate vorticity  $\xi$  and thus to calculate the circulation  $\Gamma$  defined by:

$$\Gamma = \iint_S \nabla \times \mathbf{v}^f \cdot \mathbf{n} \, dS = \iint_S \xi \cdot \mathbf{n} \, dS; \quad \xi = \nabla \times \mathbf{v}^f \quad (4)$$

where  $\mathbf{n}$  is the exterior normal unit vector. The flow rotational character is confined only to layer in contact with the blade by introducing vorticity  $\xi$  in order to model the lift in the center of each panel element.

The vector potential  $\psi$  is considered as solenoidal potential, enforcing that  $\nabla \cdot \psi = 0$ . Thus, by exploiting the results in (2) and (4), we obtain the governing equation for vector potential:

$$\xi = -\nabla^2\psi \quad (5)$$

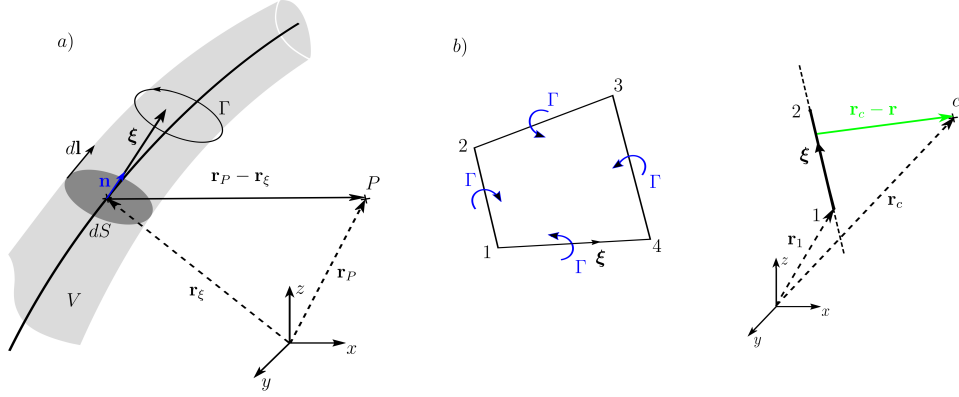


Figure 1: a) Velocity at point  $P$  induced by a vortex segment b) Velocity at the center induced by a vortex ring with constant intensity

The fundamental solution of equation (5) is obtained by using Green's function:

$$\psi = \frac{1}{4\pi} \int_V \frac{\xi}{|\mathbf{r}_\xi - \mathbf{r}_P|} dV \quad (6)$$

Here  $\psi$  is evaluated at point  $P$  defined by its position  $\mathbf{r}_P$  and is result of integrating vorticity  $\xi$  at point  $\mathbf{r}_\xi$  within the volume  $V$  (see Figure 1-a). We will consider an infinitesimal vorticity filament  $d\mathbf{l}$  with a constant circulation  $\Gamma$  and the cross section area  $dS$  in (4) that it is normal to  $\xi$ . The equation (6) can be recast as:

$$\psi = \frac{1}{4\pi} \int_l \frac{\Gamma}{|\mathbf{r}_\xi - \mathbf{r}_P|} \cdot d\mathbf{l} \quad (7)$$

Thus, the velocity induced at a point  $P$  by vorticity filament with a constant circulation  $\Gamma$  can be defined by Biot-Savart law as:

$$\nabla \times \boldsymbol{\psi} = \frac{\Gamma}{4\pi} \int_l \frac{(\mathbf{r}_\xi - \mathbf{r}_P)}{|\mathbf{r}_\xi - \mathbf{r}_P|^3} \times d\mathbf{l} \quad (8)$$

The panel method is a boundary method which only concerns the fluid-structure interface. It solves the Laplace equation (3) by superposition of singularity elements, which are also fundamental solutions to the Laplace equation. The choice of these singularity elements depends obviously on the problem to be modeled. For aerodynamic problem, the combination of free stream and vortex

rings singularities is most widely used [9]. For the case where we consider a wind turbine blade in a steady free stream, we can choose:  $\nabla\phi = \mathbf{v}_\infty$ . Thus, the result in (2) can be redefined by:

$$\mathbf{v}^f = \mathbf{v}_\infty + \mathbf{v}_d^f \quad (9)$$

where  $\mathbf{v}_d^f$  is the velocity induced by vortex rings singularities. By definition, the vortex ring is a closed contour  $C$  composed of four straight filaments with a constant strength (see Figure 1-b). The velocity induced by a vortex ring at a control point  $\mathbf{r}_c$  is derived from (8):

$$\mathbf{v}_d^f = \frac{\Gamma}{4\Pi} \int_C \frac{(\mathbf{r} - \mathbf{r}_c)}{|\mathbf{r} - \mathbf{r}_c|^3} \times d\mathbf{l} = \mathbf{v}_{d,1-2}^f + \mathbf{v}_{d,2-3}^f + \mathbf{v}_{d,3-4}^f + \mathbf{v}_{d,4-1}^f \quad (10)$$

where  $\mathbf{v}_{d,1-2}^s$  is obtained by integrating over a straight vortex filament between points '1' and '2' (see Figure 1-b):

$$\begin{aligned} \mathbf{v}_{d,1-2}^f &= \frac{\Gamma}{4\Pi} \text{geo}(\mathbf{r}_c, \mathbf{r}_1, \mathbf{r}_2) \\ &= \frac{\Gamma}{4\Pi} \frac{(\mathbf{r}_1 - \mathbf{r}_c) \times (\mathbf{r}_2 - \mathbf{r}_c)}{|(\mathbf{r}_1 - \mathbf{r}_c) \times (\mathbf{r}_2 - \mathbf{r}_c)|^2} (\mathbf{r}_2 - \mathbf{r}_1) \cdot \left( \frac{(\mathbf{r}_1 - \mathbf{r}_c)}{|\mathbf{r}_1 - \mathbf{r}_c|} - \frac{(\mathbf{r}_2 - \mathbf{r}_c)}{|\mathbf{r}_2 - \mathbf{r}_c|} \right) \end{aligned} \quad (11)$$

The position vectors  $\mathbf{r}_c$ ,  $\mathbf{r}_1$  and  $\mathbf{r}_2$  are expressed in the fixed coordinate systems. Others components of  $\mathbf{v}_d^f$  are computed in the same manner as  $\mathbf{v}_{d,1-2}^f$ .

We seek to compute the fluid velocity  $\mathbf{v}^f$  in order to deduce the aerodynamic loads by imposing the impermeability boundary condition which concerns only the normal component of the flow:

$$(\mathbf{v}^f - \mathbf{v}^s) \cdot \mathbf{n} = 0 \quad (12)$$

where  $\mathbf{v}^s$  is the structure velocity with superscript 's', indicating structure. For the rigid blades (see [1]),  $\mathbf{v}^s$  can be expressed only by the angular velocity defined as  $\boldsymbol{\Omega}^s \times \mathbf{r}$ , where  $\boldsymbol{\Omega}^s$  is the angular rotor velocity. However, in the present case where the blades are flexible,  $\mathbf{v}^s$  is also affected by the structure deformations.

In discrete approximation, the blade surface is divided into a number of panels with a control point  $c$ . A vortex ring of constant strength  $\Gamma$  is placed in the center of each panel (see Figure 2). The zero normal flow condition as

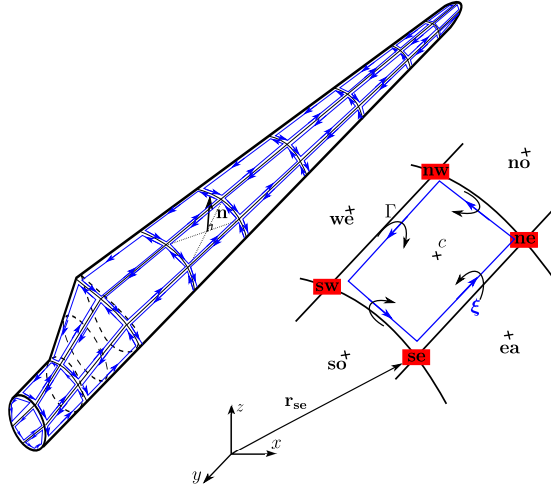


Figure 2: Blade surface discretization and vortex rings distribution

written in (12) should be satisfied at the control point  $\mathbf{r}_c^{(i)}$  of each panel ( $i$ ), considering the influence of every other panel ( $j$ ):

$$\begin{aligned} \left( \mathbf{v}^f(\mathbf{r}_c^{(i)}) - \mathbf{v}^s(\mathbf{r}_c^{(i)}) \right) \cdot \mathbf{n}_c^{(i)} &= 0 \\ \left( \mathbf{v}_\infty + \sum_{j=1}^{nb} \mathbf{a}_{i,j} \Gamma^{(j)} - \mathbf{v}^s(\mathbf{r}_c^{(i)}) \right) \cdot \mathbf{n}_c^{(i)} &= 0 \end{aligned} \quad (13)$$

where  $nb$  is the total number of blade panel elements. The vectors  $\mathbf{a}_{i,j}$  are the influence coefficients (see Figure 2), computed from (10) and (11):

$$\begin{aligned} \mathbf{a}_{i,j} = \frac{1}{4\Pi} \times & \left( geo(\mathbf{r}_c^{(i)}, \mathbf{r}_{nw}^{(j)}, \mathbf{r}_{sw}^{(j)}) + geo(\mathbf{r}_c, \mathbf{r}_{sw}, \mathbf{r}_{se}^{(j)}) \right. \\ & \left. + geo(\mathbf{r}_c^{(i)}, \mathbf{r}_{se}^{(j)}, \mathbf{r}_{ne}^{(j)}) + geo(\mathbf{r}_c^{(i)}, \mathbf{r}_{ne}^{(j)}, \mathbf{r}_{nw}^{(j)}) \right) \end{aligned} \quad (14)$$

The system is closed by enforcing the Kutta condition, which allows to pick the physically sound circulation at the sharp edge. The latter implies that the flow should leave the sharp trailing edge of an airfoil smoothly with the velocity that should remain finite. Practically, for each circulation over a row of blade panels, at the trailing edge, we add a single wake panel that allows to enforce the following condition (see Figure 3):

$$\Gamma_{T.E} = 0 \Rightarrow \Gamma_{wake} = \Gamma_{upper} - \Gamma_{lower} \quad (15)$$

Ideally the wake panels extend to infinity, but in practice we choose the length of wake panel that should be large enough to satisfy this condition. The addition of wake panels involves adding new unknowns to the system for each row of blade panels. By imposing Kutta condition and zero normal flow condition, we obtain a set of linear algebraic equations including both blade and wake circulations as unknowns:

$$\begin{bmatrix} a_{1,1} & a_{1,2} & \dots & a_{1,np} \\ a_{2,1} & a_{2,2} & \dots & a_{2,np} \\ \vdots & \vdots & \ddots & \vdots \\ a_{nb,1} & a_{nb,2} & \dots & a_{nb,np} \\ & \dots & & \\ \leftarrow \text{Kutta condition} \rightarrow & & & \\ & \dots & & \end{bmatrix} \begin{bmatrix} \Gamma^{(1)} \\ \Gamma^{(2)} \\ \vdots \\ \Gamma^{(nb)} \\ \Gamma^{(nb+1)} \\ \cdot \\ \Gamma^{(np)} \end{bmatrix} = \begin{bmatrix} (\mathbf{v}_\infty - \mathbf{v}^s(\mathbf{r}_c^{(1)})) \cdot \mathbf{n}_c^{(1)} \\ (\mathbf{v}_\infty - \mathbf{v}^s(\mathbf{r}_c^{(2)})) \cdot \mathbf{n}_c^{(2)} \\ \vdots \\ (\mathbf{v}_\infty - \mathbf{v}^s(\mathbf{r}_c^{(nb)})) \cdot \mathbf{n}_c^{(nb)} \\ 0 \\ \cdot \\ 0 \end{bmatrix} \quad (16)$$

where  $np$  is the total number of panel elements. Once we solve for  $\Gamma$  values, we can recover from (9) the fluid velocity field in the control point of each panel ( $i$ ):

$$\mathbf{v}^f(\mathbf{r}_c^{(i)}) = \mathbf{v}_\infty + \sum_{j=1}^{nb} \mathbf{a}_{i,j} \Gamma^{(j)} - \frac{1}{2} \nabla \Gamma^{(i)} \quad (17)$$

where

$$\nabla \Gamma^{(i)} \simeq \frac{\begin{bmatrix} (\mathbf{r}_{we} - \mathbf{r}_{no})(\Gamma_{we} + \Gamma_{no}) + (\mathbf{r}_{so} - \mathbf{r}_{we})(\Gamma_{so} + \Gamma_{we}) + \\ (\mathbf{r}_{ea} - \mathbf{r}_{so})(\Gamma_{ea} + \Gamma_{so}) + (\mathbf{r}_{no} - \mathbf{r}_{ea})(\Gamma_{no} + \Gamma_{ea}) \end{bmatrix} \times \mathbf{n}_c^{(i)}}{|\mathbf{r}_{no} - \mathbf{r}_{so}| \times |\mathbf{r}_{we} - \mathbf{r}_{ea}|} \quad (18)$$

The extra term  $\nabla \Gamma$  in (17) represents the tangential velocity contribution of the panel ( $i$ ) itself, obtained by using the gradient theorem and the values of  $\Gamma$  at neighboring control points (see Figure (2)).

The computed fluid velocity is written in the current deformed configuration, by using the Eulerian formulation. When computing the corresponding fluid pressure exerted on solid blades, this velocity should be transferred from the Eulerian to the Lagrangian formulations, for which we use:

$$\bar{\mathbf{v}}^f = \mathbf{v}^f - \mathbf{v}^s \quad (19)$$

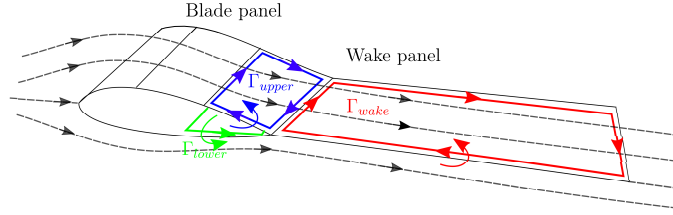


Figure 3: Kutta condition at the trailing edge

The transformation of this kind represents the fluid velocity seen by an observer located at a coordinate system attached to the blade. With this result on hand, we can further use the Bernoulli equation enforcing the energy conservation along a streamline, in order to obtain the corresponding value of pressure at the panel element ( $i$ ) which is computed at the control point in the center according to:

$$p^{(i)} = \frac{1}{2} \rho ( |\mathbf{v}_\infty|^2 - |\bar{\mathbf{v}}^f(\mathbf{r}_c^{(i)})|^2 ) \quad (20)$$

The computed pressure is normal to the panel and constant over a particular panel element. All panel values of pressure are grouped in a vector denoted by  $\mathbf{P}^f$ , and transferred to the structural solver. We ensure that the fluid and structure variables are recast in the same coordinates system. Given that fluid and structure models have the same discretization at interface, no special procedure is needed for such data transfer operation.

## 2.2. Structure model based upon 3D enhanced solid element

In this section, we present structural dynamic formulation for the wind turbine blades. The latter are modeled by the 3D solid element undergoing large displacements and large rotations. Such large overall motion is described by specifying the motion of each particle from the initial configuration  $\mathbf{x}$  to the deformed configuration  $\mathbf{x}^\varphi$  as:

$$\mathbf{x}^\varphi = \varphi(\mathbf{x}) \quad (21)$$

where  $\varphi$  is a point transformation [17]. The corresponding deformation gradient can be written as:

$$\mathbf{F} = \nabla\varphi; \quad J(\mathbf{x}) = \det[\mathbf{F}] \quad (22)$$

For a large overall motion of turbine blades, the current (deformed) and the initial (fixed) configurations are quite different. One can no longer simplify computing the derivatives and integrals in the deformed configuration with respect to the coordinates chosen in the initial configuration [17].

The weak form of the equilibrium equations is written by using the coordinates in the current configuration:

$$G(\varphi, \mathbf{u}^\varphi) = \int_{\mathbf{V}^\varphi} \boldsymbol{\varepsilon}^\varphi(\mathbf{u}^\varphi) \cdot \boldsymbol{\sigma}^\varphi \, d\mathbf{V}^\varphi - \int_{\mathbf{V}^\varphi} \mathbf{u}^\varphi \cdot \mathbf{f}^\varphi \, d\mathbf{V}^\varphi - \int_{\varphi(\mathbf{S}_p)} \mathbf{u}^\varphi \cdot \bar{\mathbf{t}}^{f,\varphi} \, d\mathbf{S}^\varphi \quad (23)$$

where  $\boldsymbol{\varepsilon}^\varphi$ ,  $\boldsymbol{\sigma}^\varphi$  and  $\mathbf{u}^\varphi$  are respectively the strain tensor, the Cauchy stress tensor and the virtual displacement vector.  $\mathbf{f}^\varphi$  and  $\bar{\mathbf{t}}^{f,\varphi}$  are the volume forces and surface forces applied to the structure. The surface force follows the normal to the surface  $\varphi(\mathbf{S}_p)$  in the current configuration, thus the name follower load. It is written as:

$$\bar{\mathbf{t}}^{f,\varphi} = p^f \mathbf{n}^\varphi \quad (24)$$

where  $\mathbf{n}^\varphi$  is the unit normal vector applied in the deformed configuration and  $p^f$  is the aerodynamic pressure computed by panel method code.

The equilibrium equation in (23) is expressed in the Eulerian description that doesn't provide any information about the deformation trajectory leading to the deformed configuration. However, the Biot strain, chosen thereafter to define the strain measures [1, 12], involves finite rotation tensor through the polar decomposition [17]. Since the finite rotations are path dependent [18, 19, 20], the Eulerian formulation must further be replaced by the Lagrangian formulation. By using the change of coordinates between the deformed and the initial configurations, we can rewrite the weak form of equilibrium equations as:

$$G(\varphi, \mathbf{u}) = \int_{\mathbf{V}} \mathbf{H}(\mathbf{u}) \cdot \mathbf{T}(\mathbf{x}) \, d\mathbf{V} - \int_{\mathbf{V}} \mathbf{u} \cdot \mathbf{f} \, d\mathbf{V} - \int_{\mathbf{S}_p} \mathbf{u} \cdot p^f J(\mathbf{x}) \mathbf{F}^{-T} \mathbf{n} \, d\mathbf{S} \quad (25)$$

where  $\mathbf{H}$  and  $\mathbf{T}$  are, respectively, the Biot strain and the Biot stress (see [12] for details). The Nanson formula [17] is used to pull-back the follower pressure boundary condition from the current configuration  $\mathbf{n}^\varphi d\mathbf{S}^\varphi$  to the initial configuration  $\mathbf{n} d\mathbf{S}$ . In order to preserve computation stability, the finite element implementation of the follower pressure is based upon the parametrization of the current surface  $\varphi(\mathbf{S}_p)$  with respect to the isoparametric domain [21]. We denote by  $\bar{\mathbf{x}}$  the position vector of a given point of  $\mathbf{S}_p$  and by  $\bar{\mathbf{x}}^\varphi$  its image in  $\varphi(\mathbf{S}_p)$ . By defining a suitable 2D domain of isoparametric parameters  $(\xi, \eta)$ , the mapping from the isoparametric domain  $\mathbf{S}_\kappa$  to the initial configuration  $\mathbf{S}_p$  is constructed by  $\kappa$ :

$$(\xi, \eta) \in \mathbf{S}_\kappa \rightarrow \bar{\mathbf{x}} = \kappa(\xi, \eta) \in \mathbf{S}_p \quad (26)$$

By exploiting results in (21) and (26), the isoparametric parametrization of the moving surface  $\varphi(\mathbf{S}_p)$  is obtained by setting  $\phi$  as:

$$(\xi, \eta) \in \mathbf{S}_\kappa \rightarrow \bar{\mathbf{x}}^\varphi = \phi(\xi, \eta) = \varphi \circ \kappa(\xi, \eta) \in \varphi(\mathbf{S}_p) \quad (27)$$

Thus, the unit normal field is expressed by using the chain rule and the isoparametric mapping:

$$\begin{aligned} \mathbf{n}^\varphi d\mathbf{S}^\varphi &= \left( \frac{\partial \phi}{\partial \xi} \times \frac{\partial \phi}{\partial \eta} \right) d\xi d\eta \\ &= \nabla \varphi(\kappa(\xi, \eta)) \frac{\partial \kappa}{\partial \xi} \times \nabla \varphi(\kappa(\xi, \eta)) \frac{\partial \kappa}{\partial \eta} d\xi d\eta \end{aligned} \quad (28)$$

With this result on hand, the weak form of the follower pressure boundary conditions defined in (23) can be written in natural coordinate system:

$$\begin{aligned} \int_{\varphi(\mathbf{S}_p)} \mathbf{u}^{s,\varphi} \cdot P^{\varphi,f} \mathbf{n}^\varphi d\mathbf{S}^\varphi &= \int_{\mathbf{S}_\kappa} \underbrace{\phi(\mathbf{u}^s) \cdot P^{\varphi,f}}_{\phi_{,\xi}(\xi, \eta)} \underbrace{\nabla \varphi(\kappa(\xi, \eta)) \frac{\partial \kappa}{\partial \xi} \times \nabla \varphi(\kappa(\xi, \eta)) \frac{\partial \kappa}{\partial \eta}}_{\phi_{,\eta}(\xi, \eta)} d\xi d\eta \\ &= \int_{\mathbf{S}_\kappa} \phi(\mathbf{u}^s) \cdot P^{\varphi,f} \phi_{,\xi}(\xi, \eta) \times \phi_{,\eta}(\xi, \eta) d\xi d\eta \end{aligned} \quad (29)$$

This kind of parametrization based on isoparametric elements is the best suited for our subsequent finite element implementation, since discretization

and linearization commute [17]. By introducing the perturbed configuration of  $\varphi$  given as:

$$\varphi_\epsilon = \varphi + \epsilon \boldsymbol{\mu}(\mathbf{x}^\varphi) = \varphi + \epsilon \boldsymbol{\mu} \circ \varphi \quad (30)$$

where  $\boldsymbol{\mu}$  is an admissible variation of  $\varphi$ , the linearization of result in (29) can be written as:

$$\begin{aligned} Lin \left[ \int_{\varphi(\mathbf{S}_p)} \mathbf{u}^{s,\varphi} \cdot P^{\varphi,f} \mathbf{n}^\varphi d\mathbf{S}^\varphi \right] &= \frac{d}{d\epsilon} \left[ \int_{\varphi(\mathbf{S}_p)} \mathbf{u}^{s,\varphi} \cdot P^{\varphi,f} \mathbf{n}^\varphi d\mathbf{S}^\varphi \right]_{\epsilon=0} \\ &= \int_{\mathbf{S}_\kappa} \boldsymbol{\phi}(\mathbf{u}^s) \cdot P^{\varphi,f} \left[ [(\nabla \boldsymbol{\mu} \circ \boldsymbol{\phi}) \boldsymbol{\phi}_{,\xi}] \times \boldsymbol{\phi}_{,\eta} + \boldsymbol{\phi}_{,\xi} \times [(\nabla \boldsymbol{\mu} \circ \boldsymbol{\phi}) \boldsymbol{\phi}_{,\eta}] \right] d\xi d\eta \end{aligned} \quad (31)$$

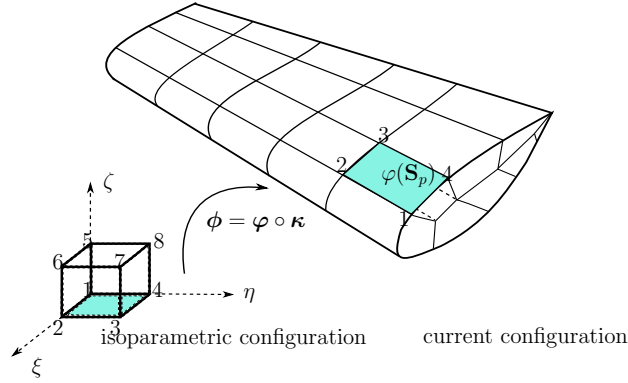


Figure 4: Choice of the finite element discretization for pressure surface

In the finite element implementation, we assume that each panel surface is a single facet of the 3D solid element used for blade modeling. The discrete approximation of the position vector in  $\varphi(\mathbf{S}_p)$  is thus constructed from the standard isoparametric interpolation of 8-nodes brick element, which results with a quadrilateral element discretization of each particular facet (see Figure 4):

$$\bar{\mathbf{x}}^\varphi = \sum_{a=1}^4 \bar{N}_a(\xi, \eta) \bar{\mathbf{x}}_a = \sum_{a=1}^4 N_a(\xi, \eta, -1) \bar{\mathbf{x}}_a \quad (32)$$

where  $N_a$  are the standard shape functions of 8-nodes brick element, while  $\bar{\mathbf{x}}_a$  are the corresponding nodal values.

By choosing the Biot strain,  $\mathbf{H} = \mathbf{R}^T(\mathbf{I} + \nabla \mathbf{u}) - \mathbf{I}$ , we introduce the finite rotation tensor  $\mathbf{R}$ , which further imposes the path-dependency. We briefly recall

the corresponding variational formulation and the discrete approximation in dynamics:

$$\begin{aligned}
i) \quad & \int_{\mathbf{V}} \delta \mathbf{u}^s \cdot \rho_s \ddot{\mathbf{u}}^s d\mathbf{V} + \int_{\mathbf{V}} \text{symm}[\mathbf{R}^{s,T} (\nabla \delta \mathbf{u}^s + (\mathbf{I} + \nabla \mathbf{u}^s + \mathbf{d}^s) \times \delta \mathbf{w}^s)] \cdot \text{symm}[\mathbf{T}] \\
& + \text{skew}[\mathbf{R}^{s,T} (\nabla \delta \mathbf{u}^s + (\mathbf{I} + \nabla \mathbf{u}^s + \mathbf{d}^s) \times \delta \mathbf{w}^s)] \cdot \text{skew}[\mathbf{T}] d\mathbf{V} \\
& - \int_{\mathbf{V}} \delta \mathbf{u}^s \cdot \mathbf{f} d\mathbf{V} - \int_{\varphi(\mathbf{S}_p)} \delta \mathbf{u}^s \cdot P^{\varphi, f} \mathbf{n}^\varphi d\mathbf{S}^\varphi = 0 \\
ii) \quad & \int_{\mathbf{V}} \{ \text{symm}[\mathbf{R}^{s,T} \delta \mathbf{d}^s] \cdot \text{symm}[\mathbf{T}] + \text{skew}[\mathbf{R}^{s,T} \delta \mathbf{P} \cdot \mathbf{d}^s] \cdot \text{skew}[\mathbf{T}] - \delta \mathbf{d}^s \cdot \mathbf{P} \} d\mathbf{V} = 0
\end{aligned} \tag{33}$$

Here  $\rho_s$  is the structure density,  $\delta \mathbf{w}$  is the axial vector associated to the infinitesimal skew-symmetric tensor  $\delta \mathbf{W}$  such that  $\delta \mathbf{W} = \delta \mathbf{R} \mathbf{R}$  and  $\delta \mathbf{W} \mathbf{b} = \delta \mathbf{w} \times \mathbf{b}$ ,  $\forall \mathbf{b} \in \mathbb{R}^3$ . The addition of an incompatible displacement gradient  $\mathbf{d}^s$  is needed to avoid locking problems. By using the finite element discretization, the variational equations in (33) is reduced to set of algebraic equations. The formulation development and the numerical implementation are presented in details in our previous work [12].

### 2.3. FSI coupling

The structural and fluid computations are performed separately and later coupled through data exchange at the fluid-structure interface. The fluid part provides the aerodynamic pressure distribution  $\mathbf{P}^f$  and the structural part provides the kinematic variables  $\mathbf{u}$  and  $\mathbf{v}$ .

The conditions to be fulfilled on the fluid-structure interface are the continuity of displacements and the surface stresses. Enforcing these conditions with the partitioned approach requires an iterative solution procedure. For a typical time step  $t_{n+1}$ , we are given the known variables  $\bar{\mathbf{x}}_n$ ,  $\mathbf{v}_n^s$ , and  $\mathbf{P}_n^f$ . We look for  $\bar{\mathbf{x}}_{n+1}$ ,  $\mathbf{v}_{n+1}^s$ , and  $\mathbf{P}_{n+1}^f$  which satisfy equations of motion for fluid, structure and interface conditions. For simplicity, we assume that the fluid and structure time steps are equal,  $\Delta t = \Delta t_s = \Delta t_f$ .

*Non-iterative procedure: conventional serial staggered procedure (CSS)*

We first consider the CSS procedure characterized by the following steps illustrated in Figure 5 :

- 1/- Transfer the kinematic variables from the structure part to fluid part and update the interface position in panel method.
- 2/- Solve the linear system (16) to compute fluid velocities  $\mathbf{v}_{n+1}^f$ . Then, compute the normal pressures vector  $\mathbf{P}_{n+1}^f$  as defined in (20).
- 3/- Transfer the pressure distribution  $\mathbf{P}_{n+1}^f$  to the structure solver where it is considered as Neumann boundary condition. It should be noted here that the benefit of choosing panel method and follower pressure boundary conditions is to allow a direct data transfer at the fluid-structure interface.
- 4/ - Apply the aerodynamic pressure  $\mathbf{P}_{n+1}^f$  on the blade surface and advance the structure system to  $t_{n+1}$  by solving the system in (33). The latter requires an iterative procedure with an implicit time integration.

The CSS scheme introduces a one time-step lag between the fluid and structure computed solutions. This can lead to an accumulation of errors and thus to a poor estimate of the computed blade response, in particular when the time-step size is not small enough. In order to compensate this time shift between the fluid and structure solvers, the predictor-corrector procedure has been proposed (e.g.[22]). The procedure involves introducing the structure displacement predictor and the pressure corrector respectively in Steps 1 and 4. It requires also a single iteration in order to provide a faster convergence. However, the choice of the prediction and correction remains unsettled issue, namely for the case of strong non-linearity. For that reason, we turn towards an iterative procedure that can converge towards the results of monolithic approach.

*Iterative procedure: generalized serial staggered procedure*

The iterative coupling algorithm is based on CSS algorithm, extended by a sub-cycling between the structure and fluid solvers until reaching convergence with the current structure motion and the corresponding aerodynamic loads. One of the convergence criterion is the aerodynamic load variation between

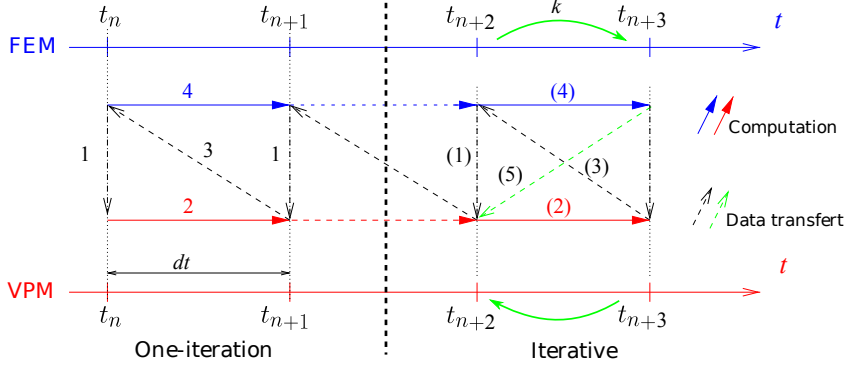


Figure 5: one-iteration (right) and iterative (left) Coupling algorithms

two iterations. Because of the large displacements and large rotations, the aerodynamic loads obtained in two different iterations are necessarily associated to two different deformed configurations. For the purpose of a fair comparison, it is convenient to transfer the pressure intensity to the initial configuration by applying an appropriate pull-back operator:

$$\tilde{\mathbf{P}}_{n+1}^{f,(k)} = \phi^*(\mathbf{P}_{n+1}^{f,(k)}) \quad (34)$$

The virtual work of fluid pressure applied on the deformed surface  $\varphi(\mathbf{S}_p)$  can be expressed as:

$$\delta \mathbf{u}^\varphi \cdot \mathbf{f}_{ext} = \int_{\varphi(\mathbf{S}_p)} \delta \mathbf{u}^\varphi \cdot p^f \mathbf{n}^\varphi d\mathbf{S}^\varphi \quad (35)$$

By reparametrizing the variation of displacement vector in the initial configuration,

$$\delta \mathbf{u}^{s,\varphi} = \delta \mathbf{u}(\varphi(\mathbf{x}^s)) = \delta \mathbf{u}(\mathbf{x}^s) \rightarrow \delta \mathbf{u}^{s,\varphi} := \delta \mathbf{u}^s \quad (36)$$

and by using the Nanson formula, (35) can be rewritten as:

$$\delta \mathbf{u} \cdot \mathbf{f}_{ext} = \int_{\mathbf{S}_p} \delta \mathbf{u} \cdot p^f \text{cof}[\mathbf{F}] \mathbf{n} d\mathbf{S}; \quad \text{cof}[\mathbf{F}] = J(\mathbf{x})\mathbf{F}^{-T} \quad (37)$$

Then, the virtual work of the fluid pressure can be directly transported in the initial configuration as follows:

$$\int_{\varphi(\mathbf{S}_p)} \delta \mathbf{u}^{s,\varphi} \cdot p^f \mathbf{n}^\varphi d\mathbf{S}^\varphi = \int_{\mathbf{S}_p} \delta \mathbf{u}^s \cdot \tilde{p}^f \mathbf{n} d\mathbf{S} \quad (38)$$

By using the transformation in (37), we obtain:

$$\int_{\mathbf{S}_p} \delta \mathbf{u}^s \cdot p^f \text{cof}[\mathbf{F}] \mathbf{n} d\mathbf{S} = \int_{\mathbf{S}_p} \delta \mathbf{u}^s \cdot \tilde{p}^f \mathbf{n} d\mathbf{S} \quad (39)$$

The pull-backed pressure for a single panel is therefore defined by:

$$\tilde{p}^f = p^f \times \|\text{cof}[\mathbf{I} + \nabla \mathbf{u}] \mathbf{n}\| \quad (40)$$

Knowing the kinetic variables and pressure distribution at time  $t_n$ , the corresponding values at time  $t_{n+1}$  are computed by solving structure motion, fluid flow and enforcing interface conditions by using the following iterative algorithm (see Figure 5):

I/- Initialize the pressure distribution for the first iteration ( $k = 0$ )

$$\mathbf{P}_{n+1}^{f,(k=0)} = \mathbf{P}_n^f \quad (41)$$

II/- Repeat the iterative procedure until the convergence, advancing at each iteration (from  $(k - 1)$  to  $(k)$ ) from (1) to (5).

(1) - The displacement vector  $\mathbf{u}_{n+1}^{(k)}$  and the velocity vector  $\mathbf{v}_{n+1}^{(k)}$ , obtained from the structure solver in the previous iteration, are transferred to the panel method code. The fluid mesh is updated to compute the corresponding pressure distribution tensor  $\mathbf{P}_{n+1}^{f,(k)}$ .

(2)- Compute the normal pressure vector  $\mathbf{P}_{n+1}^{f,(k)}$  by means of panel method code.

(3)- The pull-back operation is performed as shown in equation (40) at the control points in order to compute  $\tilde{\mathbf{P}}_{n+1}^{f,(k)}$  and the convergence pressure criterion can be checked by means of

$$\|\tilde{\mathbf{P}}_{n+1}^{f,(k)} - \tilde{\mathbf{P}}_{n+1}^{f,(k-1)}\| \leq \text{tol}_1 \quad (42)$$

(4)- The pressure distribution  $\mathbf{P}_{n+1}^{f,(k)}$  is transferred to the FEM code. An iterative resolution of the following nonlinear system is executed in order to update kinematic variables

$$\mathbf{M} \begin{bmatrix} \Delta \ddot{\mathbf{u}}_{n+1}^{s,(k)} \\ \Delta \ddot{\mathbf{w}}_{n+1}^{s,(k)} \end{bmatrix} + (\tilde{\mathbf{K}}_{n+1} + \bar{\mathbf{K}}(P_{n+1}^{\varphi,f,(k)})) \begin{bmatrix} \Delta \mathbf{u}_{n+1}^{s,(k)} \\ \Delta \mathbf{w}_{n+1}^{s,(k)} \end{bmatrix} = \mathbf{r}_{n+1} + \bar{\mathbf{r}}(P_{n+1}^{f,(k)}) \quad (43)$$

where  $\mathbf{M}$  is the mass matrix,  $\tilde{\mathbf{K}}$  is the condensed stiffness matrix and  $\bar{\mathbf{K}}$  is the stiffness matrix associated to the pressures elements.

(5)- The second convergence criterion can then be checked pertinent to the structure displacement

$$\|\mathbf{u}_{n+1}^{(k+1)} - \mathbf{u}_{n+1}^{(k)}\| \leq tol_2 \quad (44)$$

If the convergence criterions (42) and (44) are not reached, the kinetic variables are transferred again to the fluid code to continue with the next iteration ( $k+1$ ).

III/- Otherwise, we advance to the next time step.

The structure formulation involves finite rotations that are highly nonlinear and require special update procedure. For that reason, the iteration ( $k+1$ ) the computation should be carried out from the configuration at  $t_n$  which has already reached the convergence state and not from the intermediate iterative configuration  $[t_{n+1}, (k)]$ . This avoids the error introduced by the intermediate configuration which can seriously impair the quality of the computed results.

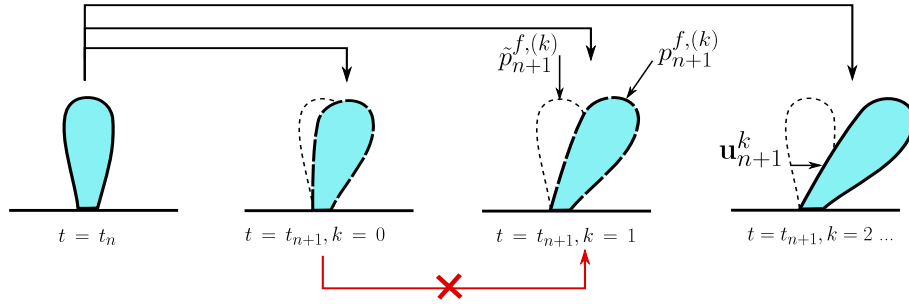


Figure 6: Robust iterative computation based on converged states

### 3. Numerical simulations of wind turbine model

In order to validate the proposed fluid-structure coupling algorithm, we consider the numerical simulation of the nonlinear dynamic response of a wind

turbine model. The latter is chosen as NREL (National Renewable Energy Laboratory) offshore 5-MW wind turbine with tests reported in [23]. It has three blade rotor with 126 m diameter. As shown in Figure 7, the blade is composed of several airfoil types described in detail in [23]. The finite element model is based on the proposed 3D solid elements. The mechanical properties are: Young's modulus  $E = 39 \text{ GPa}$ , poisson's ratio  $\nu = 0$  and mass density  $\rho = 2100 \text{ kg/m}^3$  [11].

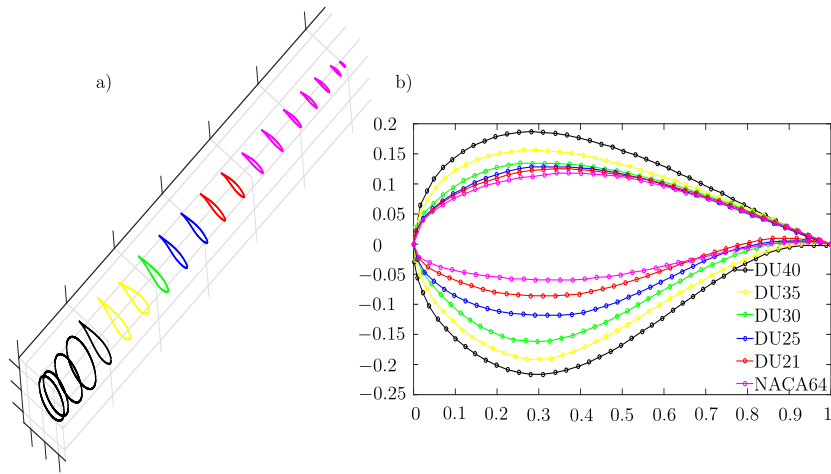


Figure 7: NREL 5-MW wind turbine model: a) positions along the span b) airfoil cross-sections in standardized code

The finite element computations are performed with a research version of the computer program FEAP, written by Prof. R.L. Taylor at UC Berkeley [24]. The panel method code is implemented with MATLAB. The data transfer is performed with MATFEAP interface.

### 3.1. Validation of the panel method

The first example concerns the validation of the aerodynamic model based on panel method. Results obtained by panel method are compared with results obtained by others aeroelastic codes such as FAST [25] and MIRAS [26]. The wind speed is ranging from  $5 \text{ m/s}$  to  $14 \text{ m/s}$ . The rotor speed is assumed to be

constant for each case.

The aerodynamics loads normal ( $F_n$ ) and tangential ( $F_t$ ) to the rotor plane are presented in Figure 15, for different values of rotation speed and wind speed. All results are computed for only one blade. The cylindrical sections of the blade doesn't provide any lift, so they are not presented in Figure 15. In general, results show that the proposed panel method code is in good agreement with the standard aeroelastic codes FAST and MIRAS. More specifically, our results are much closer to these obtained by MIRAS because both are based on an approximation of the solution of Laplace's equations using different singularities. However, the code FAST implements the BEM technique.

One can notice that the normal force is still higher than the tangential force. It increases linearly until it hits the maximum at approximately 90% of the total blade length. That can be explained with higher rotational speed at the tip of the blade ( $V_r = \Omega \times r$ ). However, the tangential force, providing the aerodynamic moment, is nearly equally distributed by means of the variation of the blade twist from 13.3 degrees at the root to the zero degrees at the tip. All results presented here allow to validate the fluid part.

Time histories of the aerodynamic torque are presented in Figure 8 in a case where the wind speed is uniform at 9 m/s and the rotor speed is 10.9 rpm. Simulations are carried for both flexible and rigid blades with a constant time step  $\Delta t = 0.01s$ . For rigid blades case, results obtained by Panel method are compared to data reported in [23], obtained by using FAST as well as the results performed by a CFD analysis in [27]. The exact match can not be expected since our computational modeling is based on different assumptions than those used in [23] and [27]. Nevertheless, the results remain rather close. The torque computed by panel method is slightly larger, which is explained by the fact that panel method doesn't take into account the drag effects.

Time histories of the aerodynamic torque are also plotted for both rigid and flexible blades in Figure 8. For rigid blade, the aerodynamic torque remains constant over time as the air flow is stationary and the rotor velocity is a constant. However, the aerodynamic torque for flexible blade, computed in the same con-

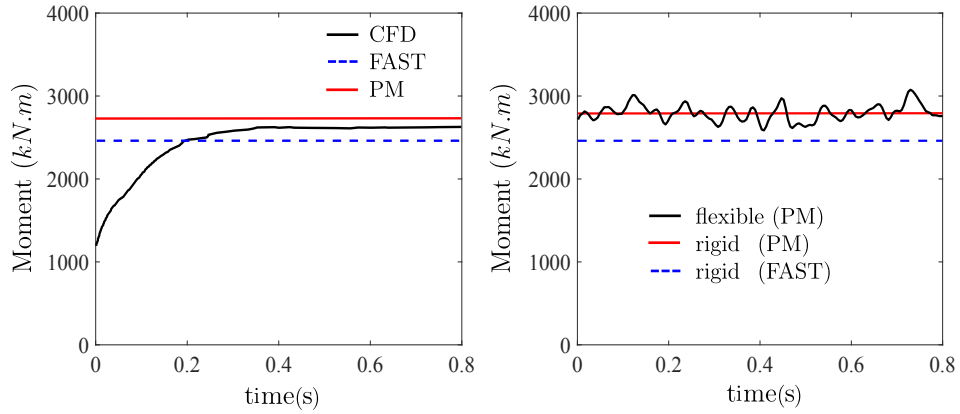


Figure 8: Time histories of the total aerodynamic torque: comparison with references for rigid blades (left) and results obtained by Panel method for both rigid and flexible blades (right)

ditions, has a tendency to oscillate due to the contribution of the deformation velocities. Therefore, the blade flexibility affects the aerodynamic loads even by imposing a constant rotor speed.

### 3.2. Coupling computations at fluid-structure interface

Next, we consider the performance of the proposed approach in handling the coupling aspects. The aerodynamic profiles and the structure proprieties remain the same as for the first example. The rotor speed is no longer constant over time. The wind turbine rotor is subject to a steady wind velocity  $11.4m/s$  and an initial rotation velocity  $12rpm$ . The simulations are carried out with a constant time step  $\Delta t = 0.05s$  by using one-iteration and iterative coupling algorithms.

The time histories of the tip blade displacements in-plane and out-plane are plotted in Figure 9. The blade mostly deforms in the flap-wise direction, which is already expected from the values of the normal loads in Figure 15. Some edge-wise deflections are also present but of much lower amplitude than the out-plane deflections. They are characterized by the presence of high frequency oscillations. We note that the in-plane and out-of-plane deflections obtained by the one-iteration algorithm are considerably larger than those obtained by

the iterative algorithm coupling. For example, the maximum of the flap-wise deflection reached by the iterative algorithm computation is nearly  $6m$ , which is consistent with the results reported in [23, 11]. However, it exceeds  $8m$  for the one-iteration coupling algorithm. We can thus deduce that the sub-cycling between structure and fluid part improves the approximation quality and avoids overestimate computed response.

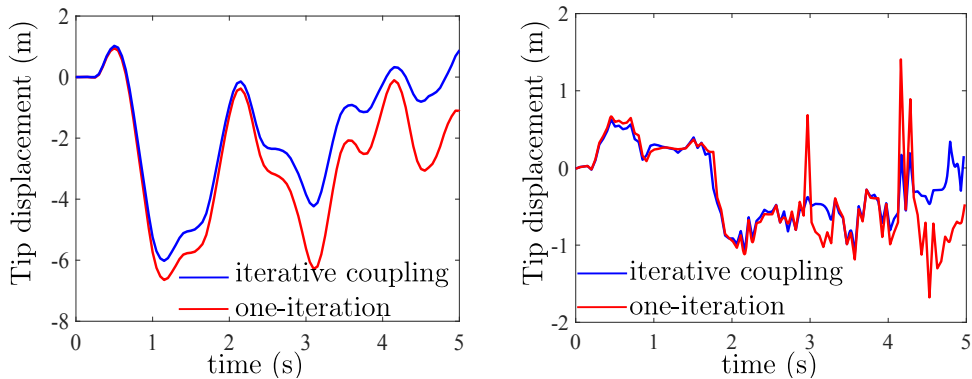


Figure 9: Time histories of the tip flap-wise (left) and edge-wise (right)

Besides, time histories of the twist angle at five different cross-sections along the blade are presented in Figure 10. They show the presence of high frequency vibrations. The twist angle characterizes the torsional deformation of airfoil sections. It increases with distance from the root because the aerodynamic forces is higher near the blade tip (see Figure 15). Between the time points  $t = 2s$  and  $t = 3.5s$ , the twist angle is negative for different cross-sections. By summing torsional deformations and aero twist angles imposed initially by the blade geometry, the total twist angle tends towards zero at different cross-sections. This will reduce the aerodynamic performance of the blade and correspondingly decrease the rotation speed of the rotor.

The major advantage of the proposed aeroelastic model is in very rapid convergence as shown in Figure 11. For a time step equal to  $0.05s$ , the number of coupling iterations remains under 10. The convergence is checked in both structure and fluid codes. The convergence displacement criterion is reached

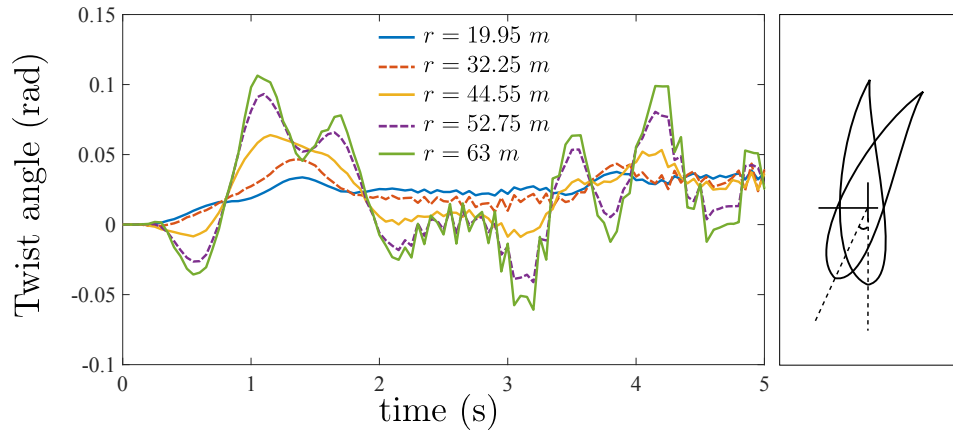


Figure 10: Time histories of the twist angle at five different cross-sections in the radial direction of the rotor

faster than the convergence pressure criterion (see Figure 11). For a given coupling iteration, the structure solver ensures quadratic convergence. The iteration number doesn't exceed 12 iterations with a satisfying rate of convergence ( $\approx 10^{-20}$ ). For the panel method code, a single iteration is sufficient to recover the aerodynamic pressure since the system to solve is linear. For a time step with six coupling iteration, the computation time is equal to 47s with Intel Core 7-8550U CPU 1.80 GHz. In Figures 9 and 10, the computed in-plane

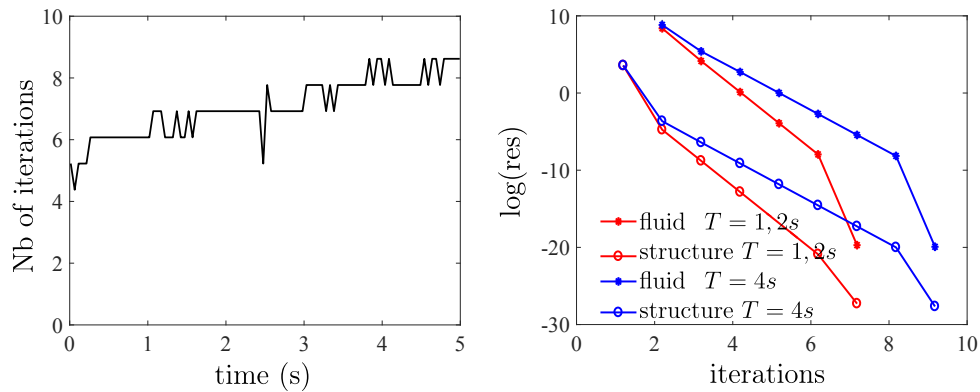


Figure 11: Coupling convergence information

displacement and the twist displacement show the presence of high frequency modes, superposed on top of low frequencies modes. The latter leads to the well known stiff system of equations, which is difficult to solve by using the standard Newmark scheme. For that, we propose to the energy-conserving time-stepping scheme, which is appropriate for such problems. The details of constructing such time stepping scheme are presented in our previous work [28]. For a time step equal to  $\Delta t = 0.01s$ , the computation using the Newmark scheme can no longer converge for time exceeding  $T = 12s$ . However, the energy conserving scheme ensures the convergence over long time interval (see Figure 12). It can avoid the instability issues of high frequencies and carry out long term simulation, which is needed for the studies of fatigue failure.

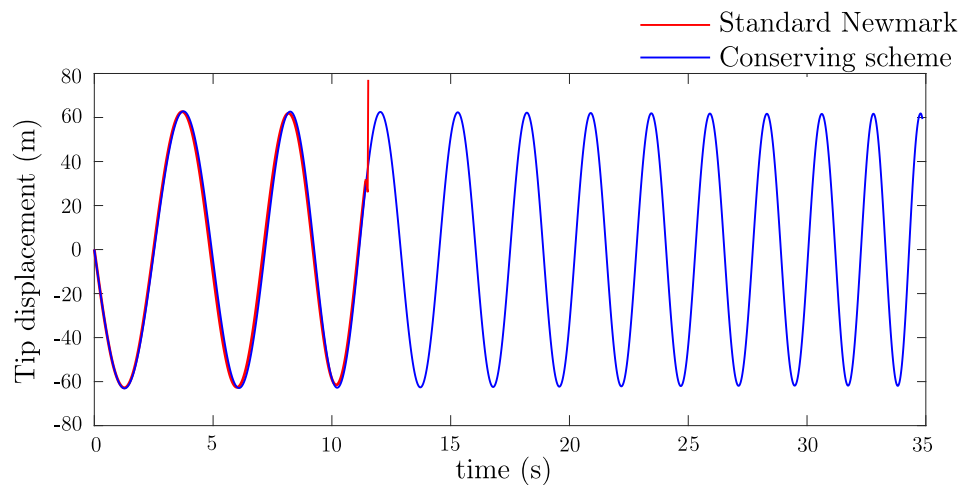


Figure 12: Time history of tip displacement in  $x$ -direction (see Figure 13): long term simulation by using energy conserving scheme

### 3.3. Computed response for pre-bent blades

Increasing blade size makes it necessary to review blade design in order to avoid peak material stresses and fatigue failures. Preliminary simulations for testing new configurations is therefore crucial and it can be established by the

proposed aeroelastic model. In this context, new configurations in terms of blade geometry and its exposure to the wind flow are tested.

As shown above, the blade bends mainly in wind direction, even risking to strike the tower and damage the system. In order to avoid such a situation, the blade can be pre-bent at an angle  $\theta$  equal to 10 deg while keeping the wind in up direction. Alternatively, we can change the blade orientation with respect to the wind direction so that the blade receives the wind in the back side of the turbine (see Figure 14).

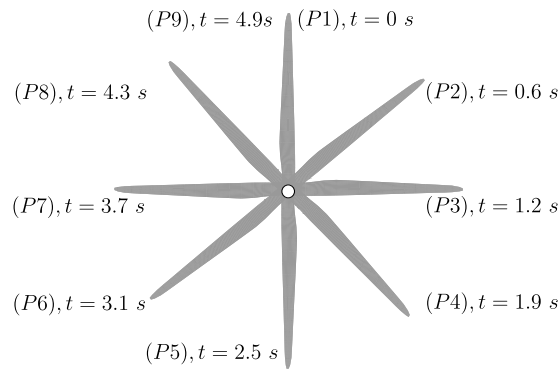


Figure 13: Blade position at several time instants during the simulation

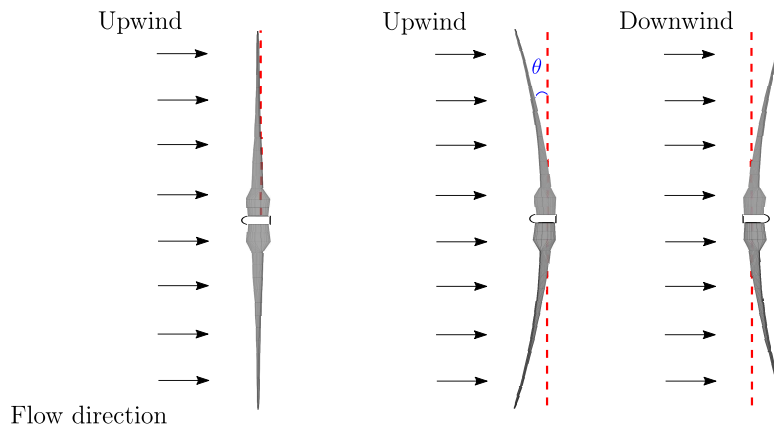


Figure 14: New configurations of blade shape and its emplacement with to wind

The von Mises stress distribution for the pre-bent downwind blade and the conventional upwind blade are plotted in Figure 16 at different calculation times (see Figure 13). As expected, the conventional blade stresses are concentrated at the bottom of the blade, which explains the succession of cylindrical profiles at the bottom of the blade in order to reinforce the structure. The stresses are also increasing in time. In fact, the wind turbine starts accelerating in time and the rotation velocity increases in time, leading to higher aerodynamic pressure and as a consequence to higher stress distribution. However, for the downwind blade, stresses are distributed uniformly indicating the benefit of such configuration. Besides, the maximum value of stress for the pre-bent downwind blade does not exceed  $4 \times 10^8 Pa$ . However, the maximum value of stress for conventional blade is equal to  $1 \times 10^{11} Pa$ . We can deduce that the downwind configuration reduces significantly the stress values.

Time histories of the flap-wise deflection and the  $x$ -displacement of the blade tip are plotted in Figure 17 for the three configurations treated here. For the upwind configuration, the conventional and the pre-bent upwind blades behave almost in the same way. The flap-wise deflection curves show the presence of a constant amplitude shift between the conventional and the pre-bent upwind blades while keeping the same oscillation modes. This shift reduces the risk of collision between the flexible blade and the tower in the upwind pre-bent configuration.

The downwind pre-bent blade presents a different flap-wise deflection response. In fact, the blade bends in the wind direction then remains in the same position with low amplitude vibrations. However, the blade rotation becomes slower because of the decrease of the tangential force in this configuration. Thus, the downwind conception is beneficial in the flexible blades case since it allows to get more homogeneous stress distribution and to avoid the risk of collision between the blade and the tower. But it implies a decrease in the aerodynamic torque which affects the wind turbine productivity.

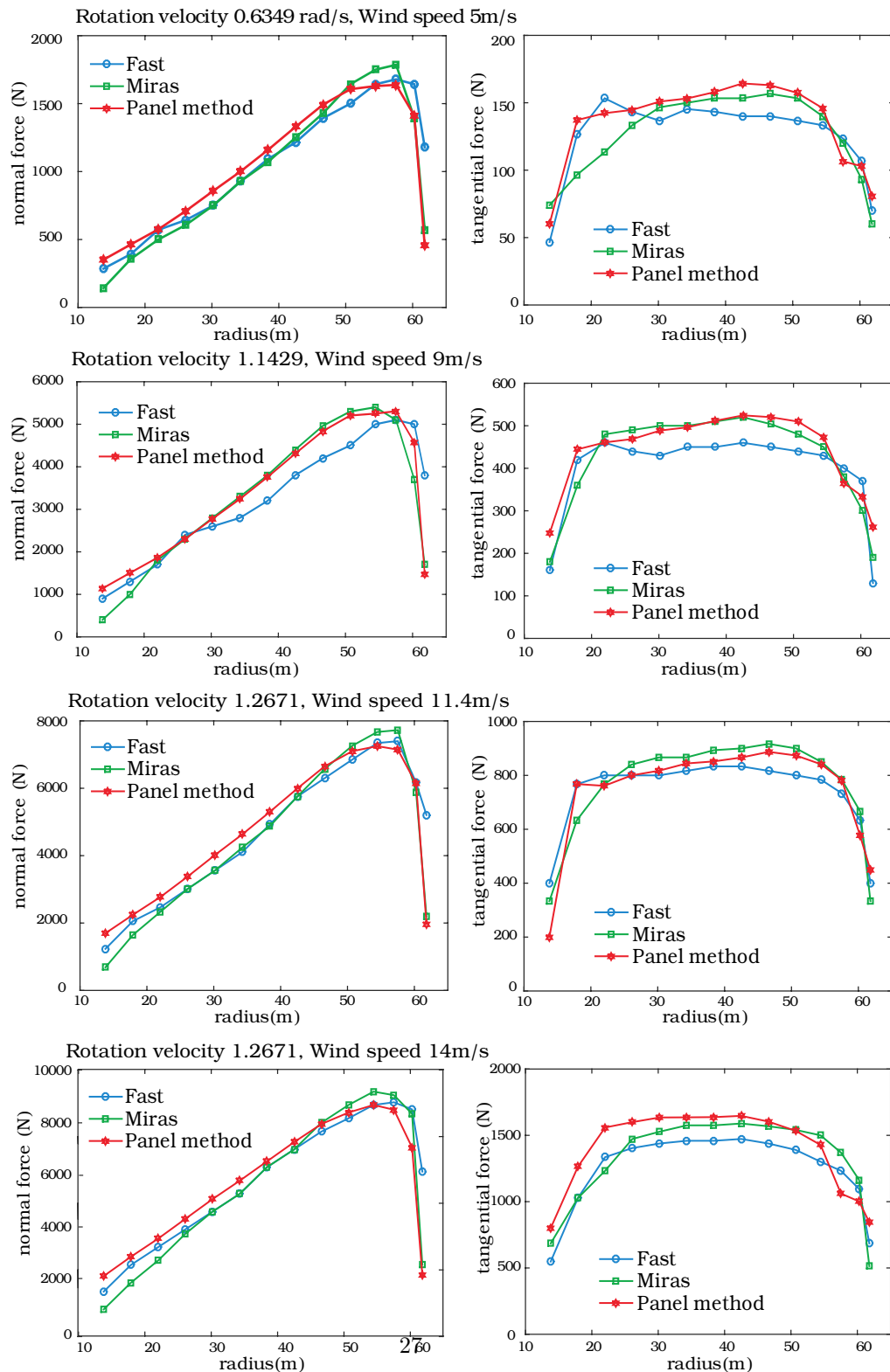


Figure 15: Comparison of the aerodynamic loads (for a single blade) normal (left) and tangential (right) to the rotor blade computed by our panel method code, FAST and MIRAS

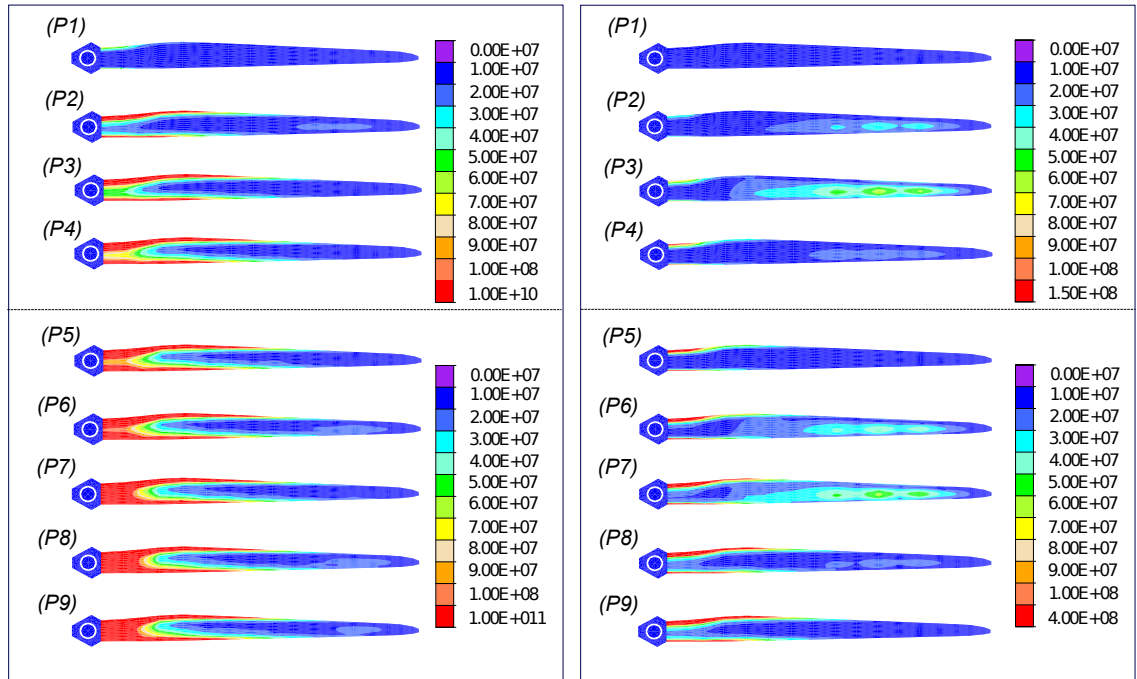


Figure 16: Comparison of Von Mises stresses distribution for conventional upwind blade (right) and downwind placement with the wind in the back (left)

#### 4. Conclusions

In this paper we present a numerical model for fluid-structure interaction capable of handling nonlinear dynamic analysis of very large wind turbines with flexible blades that can deflect significantly under wind loading. The model is based on an efficient partitioned approach to fluid-structure interaction (FSI) considering incompressible and non-viscous flow interacting with a flexible 3D blade structure undergoing overall large transformations. It seeks to provide a good estimate to the aerodynamic loads and the associated dynamic response of such structure with relatively little computation effort which is of interest for preliminary design phase.

The choice of the 3D solid element to model the flexible wind turbine blades provides a more detailed information on the stress distribution in the blades

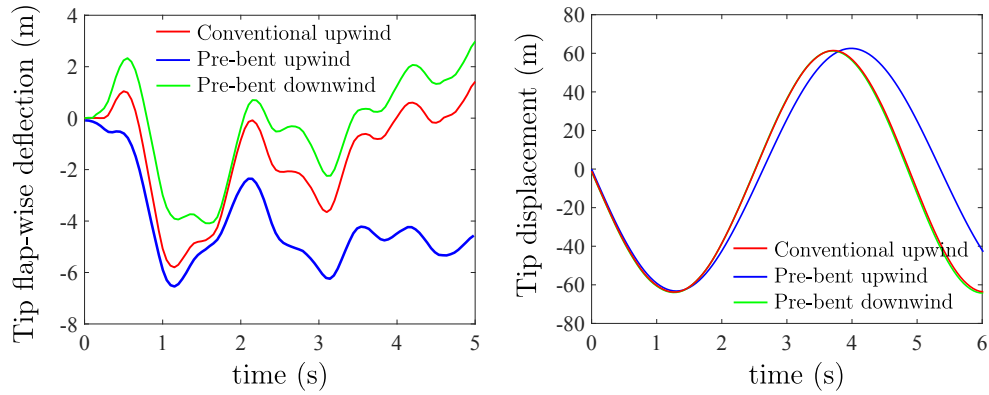


Figure 17: Comparison between conventional upwind blade, pre-bent upwind blade and pre-bent downwind blade: time histories of the tip flap-wise direction (right) and tip displacement in  $x$ -direction (left)

than what could be obtained from standard structural models, such as beam and shells, in general used for this purpose. Such more detailed stress distribution is of special interest for studies of risk of fatigue failure, which is the principal cause of failure for wind turbine blades. In order to improve the bending approximation, the proposed solid element is enhanced by a special choice of deformation incompatible modes. The solid element computations are performed by a research version of computer code FEAP.

The fluid model is based on 3D vortex panel method. It consider the fluid flow representation only on the solid boundary, resulting with relatively fast method for calculating the pressure distribution compared to CFD solution to full Navier-Stokes equations, yet it provides comparable results for the blades torque. The latter is recovered by taking into account the vorticity and the Bernoulli momentum conservation along the streamlines. An efficient iterative procedure ensures a simple data exchange between fluid and structure, mostly thanks to using 3D solid finite elements that enforce the mesh conformity. The aerodynamic and structural domains interact with each other via a partitioned coupling scheme with iterative procedure, where special provisions are taken in order to account for large overall motion.

The perspective of this work is in studying fatigue failure under variable wind loads, where the proposed panel model should be extended to non-stationary flows and unsteady Bernoulli relation. This will enable us to model wind turbine blades behavior under challenging wind conditions, such as sudden wind gust.

## 5. Acknowledgments

This work was supported by the French Ministry of Higher Education and Research, as well as the funding by Regional government and EU for Chair of Computational Mechanics. This support is gratefully acknowledged. The authors would also like to thank the Professors William Devenport (Virginia Polytechnic) who provided us with a preliminary version of the panel method MATLAB code.

## References

- [1] A. Ibrahimbegovic, A. Boujelben, Long-term simulation of wind turbine structure for distributed loading describing long-term wind loads for preliminary design, *Coupled systems mechanics* 7 (2017) 233–254.
- [2] F. Shakib, T. Hughes, Z.Johan, A new finite element formulation for computational fluid dynamics: X. the compressible euler and navier-stokes equations, *Computer Methods in Applied Mechanics and Engineering* 89 (1991) 141–219.
- [3] X. Wang, K. J. Bathe, Displacement pressure based mixed finite element formulations for acoustic fluidstructure interaction problems, *International Journal for Numerical Methods in Engineering* 40 (1997) 2001 – 2017.
- [4] L. G. Olson, K. J. Bathe, Analysis of fluid-structure interactions. a direct symmetric coupled formulation based on the fluid velocity potential, *Computers and Structures* 21 (1) (1985) 21 – 32.

- [5] J. Degroote, K. J. Bathe, J. Vierendeels, Performance of a new partitioned procedure versus a monolithic procedure in fluid–structure interaction, *Computers and Structures* 87 (2009) 793–801.
- [6] H. Glauret, Airplane propellers, *Aerodyn Theory* 4 (1935) 169–360.
- [7] K. Bathe, H. Zhang, A mesh adaptivity procedure for cfd and fluid-structure interactions, *Computers and Structures* 87 (11) (2009) 604 – 617.
- [8] C. Nitikitpaiboon, K. J. Bathe, An arbitrary lagrangianeulerian velocity potential formulation for fluidstructure interaction, *Computers and Structures* 47 (1993) 871 – 891.
- [9] J. Katz, A. Plotkin, *Low Speed Aerodynamics* (Cambridge Aerospace Series), Cambridge university press, 2001.
- [10] L. Wang, X. Liu, N. Renevier, M. Stables, G. M. Hall, Nonlinear aeroelastic modelling for wind turbine blades based on blade element momentum theory and geometrically exact beam theory, *Energy* 76 (2014) 487–501.
- [11] Y. Bazilevs, M. Hsu, J. Kiend, R. Wüchner, K. Bletzinger, 3d simulation of wind turbine rotors at full scale. part ii: Fluid–structure interaction modeling with composite blades, *International Journal for Numerical Methods in Fluids* 65 (2011) 236–253.
- [12] A. Boujelben, A. Ibrahimbegovic, Finite-strain three-dimensional solids with rotational degrees of freedom: non-linear statics and dynamics, *Advanced Modeling and Simulation in Engineering Sciences* 4 (2016) 646–654.
- [13] C. Felippa, K. Park, Staggered transient analysis procedures for coupled mechanical systems: Formulation, *Computer Methods in Applied Mechanics and Engineering* 24 (1980) 61–111.
- [14] L. J. Hess, Panel methods in computational fluid dynamics, *Annu. Rev. of Fluid Mech* 22 (1990) 255—274.

- [15] L. J. Hess, A. M. O. Smith, Calculation of potential flow about arbitrary bodies, Progress in Aerospace Science 8.
- [16] G. Arfken, Helmholtz's Theorem, Sec1.15 in Mathematical Methods for Physicists, 3rd ed. Orlando, FL: Academic Press, 1985.
- [17] A. Ibrahimbegovic, Nonlinear solid mechanics: theoretical formulations and finite element solution methods, Springer Science and Business Media, 2009.
- [18] A. Ibrahimbegovic, F. Frey, I. Kozar, Computational aspects of vector-like parametrization of three-dimensional finite rotations, International Journal of Numerical Methods in Engineering 38 (1995) 3653–3673.
- [19] A. Ibrahimbegovic, On the choice of finite rotation parameters, International Journal for Numerical Methods in Engineering 149 (1997) 49–71.
- [20] A. Ibrahimbegovic, M. A. Mikdad, Finite rotations in dynamics of beams and implicit time-stepping schemes, International Journal for Numerical Methods in Engineering 41 (1998) 781–814.
- [21] J. Simo, R. Taylor, P. Wriggers, A note on finite-element implementation of pressure boundary loading, Communications in Applied Numerical Methods 7 (1991) 513–525.
- [22] S. Piperno, C. Farhat, B. Larrouturou, Partitioned procedures for the transient solution of coupled aeroelastic problems, Computational Methods Appl. Mech. Eng 124 (1995) 79–112.
- [23] J. Jonkman, S. Butterfield, W. Musial, G. Scott, Definition of a 5-MW reference wind turbine for offshore system development, Technical Report NREL/TP-500-38060 National Renewable Energy Laboratory, Golden, C, 2009.
- [24] O. Zienkiewicz, R. Taylor, The Finite Element Method: Basic Formulation and Linear Problems, Vol. I, McGraw-Hill, Maidenhead, U.K, 1989.

- [25] J. Jonkman, J. Buhl, M. I. fast user's guide, nrel/el-500-38230 (previously nrel/el-500-29798), Golden, CO: National Renewable Energy Laboratory.
- [26] M. Sessarego, H. Y. N. Ramos-Garcia, W. Z. Shen, Aerodynamic wind-turbine rotor design using surrogate modeling and three-dimensional viscous-inviscid interaction technique, *Renewable Energy* 93 (2016) 620–635.
- [27] Y. Bazilevs, M. Hsu, I. Akkerman, S. Wright, K. Takizawa, B. Henicke, T. Spielman, T. E. Tezduyar, 3d simulation of wind turbine rotors at full scale. part i: Geometry modeling and aerodynamics, *International Journal for Numerical Methods in Fluids* 65 (2011) 207–235.
- [28] A. Boujelben, A. Ibrahimbegovic, Conserving and decaying energy for finite-strain three-dimensional solids with rotational degrees of freedom in nonlinear dynamics, *Comptes rendus Mecanique* 346 (2018) 571–580.